Experimental room temperature hohlraum performance study on the National Ignition Facility

J. E. Ralph, D. Strozzi, T. Ma, J. D. Moody, D. E. Hinkel, D. A. Callahan, B. J. MacGowan, P. Michel, J. L. Kline, S. H. Glenzer, F. Albert, L. R. Benedetti, L. Divol, A. J. MacKinnon, A. Pak, J. R. Rygg, M. B. Schneider, R. P. J. Town, K. Widmann, W. Hsing, and M. J. Edwards

Citation: Phys. Plasmas **23**, 122707 (2016); doi: 10.1063/1.4972548

View online: http://dx.doi.org/10.1063/1.4972548

View Table of Contents: http://aip.scitation.org/toc/php/23/12

Published by the American Institute of Physics

Experimental room temperature hohlraum performance study on the National Ignition Facility

J. E. Ralph,[1] D. Strozzi,[1] T. Ma,[1] J. D. Moody,[1] D. E. Hinkel,[1] D. A. Callahan,[1] B. J. MacGowan,[1] P. Michel,[1] J. L. Kline,[2] S. H. Glenzer,[3] F. Albert,[1] L. R. Benedetti,[1] L. Divol,[1] A. J. MacKinnon,[3] A. Pak,[1] J. R. Rygg,[1] M. B. Schneider,[1] R. P. J. Town,[1] K. Widmann,[1] W. Hsing,[1] and M. J. Edwards[1]
[1]*Lawrence Livermore National Laboratory, Livermore, California 94550, USA*
[2]*Los Alamos National Laboratory, Los Alamos, New Mexico 87545, USA*
[3]*SLAC National Accelerator Laboratory, Menlo Park, California 94025, USA*

(Received 16 September 2016; accepted 5 December 2016; published online 29 December 2016)

Room temperature or "warm" (273 K) indirect drive hohlraum experiments have been conducted on the National Ignition Facility with laser energies up to 1.26 MJ and compared to similar cryogenic or "cryo" (~20 K) experiments. Warm experiments use neopentane (C_5H_{12}) as the low pressure hohlraum fill gas instead of helium, and propane (C_3H_8) to replace the cryogenic DT or DHe3 capsule fill. The increased average Z of the hohlraum fill leads to increased inverse bremsstrahlung absorption and an overall hotter hohlraum plasma in simulations. The cross beam energy transfer (CBET) from outer laser beams (pointed toward the laser entrance hole) to inner beams (pointed at the equator) was inferred indirectly from measurements of Stimulated Raman Scattering (SRS). These experiments show that a similar hot spot self-emission shape can be produced with less CBET in warm hohlraums. The measured inner cone SRS reflectivity (as a fraction of incident power neglecting CBET) is ~2.5× less in warm than cryo shots with similar hot spot shapes, due to a less need for CBET. The measured outer-beam stimulated the Brillouin scattering power that was higher in the warm shots, leading to a ceiling on power to avoid the optics damage. These measurements also show that the CBET induced by the flow where the beams cross can be effectively mitigated by a 1.5 Å wavelength shift between the inner and outer beams. A smaller scale direct comparison indicates that warm shots give a more prolate implosion than cryo shots with the same wavelength shift and pulse shape. Finally, the peak radiation temperature was found to be between 5 and 7 eV higher in the warm than the corresponding cryo experiments after accounting for differences in backscatter. *Published by AIP Publishing.*
[http://dx.doi.org/10.1063/1.4972548]

I. INTRODUCTION

In an indirect drive inertial confinement fusion (ICF), high power lasers are used to heat the interior of a high Z hollow cylinder known as a hohlraum. The hohlraum produces a nearly blackbody distribution of x-rays that remain partially trapped inside the hohlraum. This ablates the outer surface of a low-Z capsule containing the fusion fuel (typically DT), which then implodes.[1–3] The highest quality implosion occurs when the x-rays uniformly ablate the capsule resulting in spherically symmetric compression. In cryogenic (or "cryo") targets fielded between 18 and 31 K, helium is used to tamp the inward expansion of the hohlraum wall and blowoff from the ablating capsule. These experiments require sophisticated targets designed to control the heat flow and take more time to field because of the cooling. One strategy to increase the rate of hohlraum experiments is to field the surrogate room-temperature (or "warm") targets. These are used to develop new measurement techniques and diagnostics, and to test new hypotheses.

The primary physics difference between warm and cryo experiments is the fill gases. The helium density used to fill the hohlraum in cryo experiments corresponds to a warm pressure far beyond the tolerance of the laser entrance hole (LEH) windows. We therefore use neopentane (C_5H_{12}) with the same fully ionized electron density as the cryo He fill. The higher average charge state Z of the warm fill leads to somewhat higher electron temperatures. We address here, the laser propagation and hohlraum performance during the peak power portion of the National Ignition Facility (NIF) laser pulse and not the earlier lower power epochs.[6] The empirical model of Stimulated Raman Scattering (SRS) presented here indicates that the warm experiments have a lower reflectivity for the same power than cryo experiments. The plastic or CH (glow discharge polymer) capsule cannot hold the high pressure DHe3 fill used in cryo shots without leakage, so we use propane (C_3H_8) with the same fully ionized electron density instead. We sometimes use deuterated propane (C_3D_8) in order to obtain the fusion neutrons for diagnostic purposes. The large amount of C in the capsule fill reduces the temperature compared to cryo fills, due to the increased radiative loss.

This paper presents experiments performed on the National Ignition Facility (NIF)[4] using gold hohlraums with CH capsules[5] and with total energies ranging from 866 kJ to 1.26 MJ. A 4-shock or "low-foot" laser pulse, designed to

put the DT fuel on a low adiabat, was used. An overview of the experiment is illustrated in Fig. 1. The upper left (right) side shows the material composition in simulations of a cryo (warm) shot. The lower half of Fig. 1 shows the beams and lower hemisphere diagnostics. The two cones of inner beams, incident at polar angles $\theta = 23.5°$ and 30°, are pointed near the hohlraum equator. The outer beams ($\theta = 44.5°$ and 50°) are pointed near the LEH. Full aperture backscatter stations (FABS) and near-backscatter imagers (NBI) collect light from stimulated Raman scattering (SRS) and stimulated Brillouin scattering (SBS), and the static x-ray imager (SXI) images in the hohlraum interior. A gated x-ray framing camera (GXD) is used to image the capsule self emission or backlit in-flight shape.

In this paper, we show that a similar implosion shape can be produced with a less inner beam power in a warm than in a comparable cryo hohlraum. These shots all use the substantial cross beam energy transfer (CBET) to the inner beams to control the shape, though less is needed in the warm shots. CBET has been used to control the shape since the start of ignition experiments in 2009, by setting the wavelength shift $\Delta\lambda \equiv \lambda_{in} - \lambda_{out}$ (quoted before frequency tripling) between the NIF's inner and outer cones. Because the warm shots use less CBET, they give a less inner beam backscatter and have improved the laser coupling to the hohlraum. The reduced CBET is supported by measurements

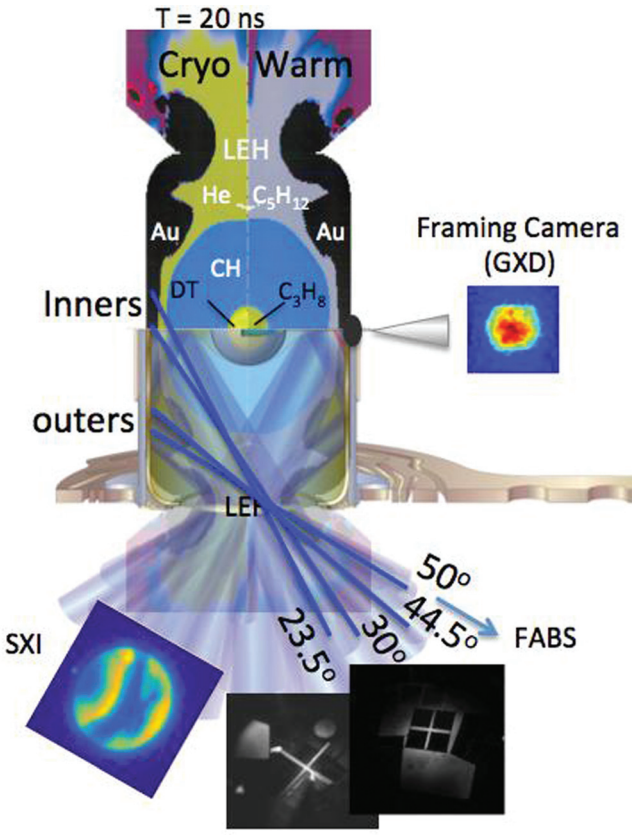

FIG. 1. Overview of experimental setup, hohlraum, and laser beams. The upper half of the hohlraum shows material regions from hydrodynamic simulations during peak power (20 ns). The black area is the gold wall. The diagnostics shown include the backscatter diagnostics (SRS and SBS), the static x-ray imager (SXI), and the polar and equatorial gated x-ray framing cameras (GXD).

of inner cone SRS, and images of the ~5 keV x-ray emission from the laser spots on the hohlraum interior. With this understanding of CBET, we conclude that the inner beam SRS reflectivity is slightly lower in these warm experiments compared to cryo ones, and that the outer beam SBS reflectivities are similar in warm and cryo experiments, *at the same post-CBET power*. In addition, the measured radiation temperature in warm experiments is 5 to 7 eV higher than in cryo experiments with similar laser pulses. This indicates that less energy is required to produce the same x-ray drive on the capsule.

Finally, these findings are supported by a direct warm-cryo comparison experiment conducted in smaller spatial scale targets. The results show that despite the warm and cryo experiments having the same inner beam cone fraction, the in-flight and hotspot shapes were both more prolate in the warm experiment. This is consistent with the full scale experiments indicating an improved propagation of the inner beams at the same power level.

This paper is organized as follows. In Section II, the warm experiment design considerations are summarized along with hydrodynamic simulation results comparing the plasma conditions of warm and cryogenic hohlraums. In Section III, the measured backscatter and the method used to infer the CBET is described. The results are compared with the published cryogenic experimental results. Section IV describes the results of the symmetry experiments conducted in warm hohlraums. Section V reviews the experimental implosion shape and Laser Plasma Interactions (LPI) of the direct warm—cryogenic experiments conducted in smaller scale hohlraums. We conclude in Section VI.

II. ROOM TEMPERATURE HOHLRAUM DESIGN AND PLASMA CONDITIONS

The warm platform was developed using the radiation-hydrodynamics code HYDRA,[7] and the standard LLNL "high flux model"[8] of detailed configuration accounting (DCA) nonlocal thermal equilibrium (NLTE) atomic physics and an electron flux limiter of 0.15 as the "free-streaming" value $n_e T_e^{3/2}/m_e^{1/2}$. The goal was to qualitatively match the hohlraum plasma conditions and x-ray drive in cryo experiments. The first few NIF hohlraum experiments in 2009 were warm, after which all experiments were cryo until the end of 2012.[9] Design work for the 2009 experiments showed that a neopentane hohlraum fill with the same fully ionized electron density as the cryo helium fill gave good surrogacy. In particular, the calculated linear gain exponents for SRS and SBS were similar, suggesting that the warm hohlraum experiments were good LPI surrogates.[10]

The blue curve in Fig. 2 shows a typical "low foot" or low adiabat pulse shape for cryo experiment N111109.[11] The laser pulses used in the warm experiments are based on this design and are shown in black and red in Fig. 2. In these experiments, the peak power into the hohlraum was ~360 TW. This is below the typical 420 TW in the comparable cryo experiments because of the risk of damage to optics from SBS. To maintain the same x-ray flux during the early time "picket," the warm pulse is of a higher power to

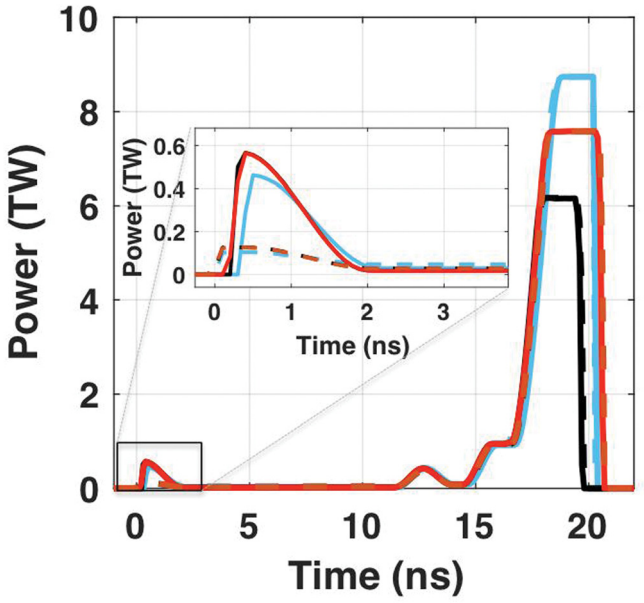

FIG. 2. Laser power per quad used in full-scale warm and cryo NIF experiments. Black and red curves are for warm shots N121226 and N130405 respectively. Blue curve is cryo shot N111109. (Dashed, solid) curves are (inner, outer) cones. The inset highlights differences between the warm and cryo pulses in the picket and trough epochs.

compensate for the higher inverse bremsstrahlung (IB) absorption and higher ionization energy compared to helium. We also reduced the warm power in the subsequent "trough" epoch to maintain the same x-ray flux as the cryo design.

The low-adiabat cryo designs use 0.96 mg/cm^3 helium hohlraum fill to tamp the inward expansion of the hohlraum wall. This helium density has the same fully ionized electron density as 0.82 mg/cm^3 of C_5H_{12}, which corresponds to a pressure of 208 Torr at room temperature (well below the tolerance of the LEH windows). The capsules on warm shots were filled with either C_3H_8 or C_3D_8, and at mass densities of 3 to 6 mg/cm^3.

Choosing warm fill densities to match the cryo n_e should give similar, though not identical, hohlraum plasma evolution. The pressure exerted on the wall by the hohlraum plasma is $n_eT_e + \sum_i n_iT_i$, with $n_e \approx \sum_i Z_i n_i$ the electron density, and (T_e, T_i) the (electron, ion) temperature. Typically $T_i < T_e$, and therefore the electron pressure dominates. Thus at the same n_e and T_e, the wall tamping in warm and cryo experiments is similar. The different charge states of the warm and cryo fills, however, give a different inverse bremsstrahlung (IB) absorption and the electron thermal conductivity. We expect T_e to be higher with a higher Z fill, since IB increases with Z and decreases with T_e, while the thermal conduction behaves oppositely. We estimate this with a simple channel-balance model, where a laser-heated channel is surrounded by a cooler "wall." We use a simplified electron energy equation, which includes the thermal conduction and IB heating

$$\frac{3}{2}\frac{\partial n_eT_e}{\partial t} - \nabla\cdot[\kappa_e\nabla T_e] = \kappa_{IB}I. \tag{1}$$

The power density absorbed by the electrons from a laser of intensity I is $\kappa_{IB}I$, with an absorption coefficient

$$\kappa_{IB} = \frac{4(2\pi)^{1/2}}{3}\frac{u_e^2}{cm_e^{1/2}}\frac{n_e^2Z_{\rm eff}L}{\eta n_{cr}T_e^{3/2}}, \tag{2}$$

$$Z_{\rm eff} \equiv \frac{\sum_i F_iZ_i^2}{\sum_i F_iZ_i}, \tag{3}$$

$\eta = [1 - n_e/n_{cr}]^{1/2}$, n_{cr} the laser critical density, $F_i = n_i/n_I$ where $n_I \equiv \sum_i n_i$ is the total ion density, $u_e \equiv e^2/4\pi\epsilon_0$, and we assume the same Coulomb logarithm L for all ion species, and for absorption and thermal conduction. The electron thermal conductivity κ_e is given by the Spitzer-Härm expression

$$\kappa_e = \frac{16\sqrt{2}}{\pi^{3/2}}\frac{T_e^{5/2}S}{m_e^{1/2}u_e^2Z_{\rm eff}}. \tag{4}$$

$S(Z_{\rm eff}) \le 1$ accounts for reduction in κ_e due to electron-electron collisions ($S = 1$ for $Z_{\rm eff} \to \infty$). We assume the steady-state $\partial/\partial t = 0$, and estimate ∇^{-2} to be the laser beam area A, to find

$$\kappa_eT_e = \kappa_{IB}P_L, \tag{5}$$

where $P_L = IA$ is the laser power. We also assume the pressure balance between the channel electrons and a specified surrounding "wall" pressure p_w, which gives $n_e = p_w/T_e$. We solve for T_e

$$T_e^7 = \frac{\pi^2}{12}\frac{u_e^4}{c\eta n_{cr}}P_LSZ_{\rm eff}^2p_w^2. \tag{6}$$

In practical units, for a 351 nm laser light

$$T_e[{\rm eV}] = 440[P_L[{\rm TW}]SZ_{\rm eff}^2p_w^2[{\rm Mb}]/\eta]^{1/7}. \tag{7}$$

As expected, this simple model implies that T_e increases with $Z_{\rm eff}$, though the dependence is fairly weak: $T_e \propto Z_{\rm eff}^{2/7}$. For fully ionized He (cryo fill) and C_5H_{12} (warm fill), we find $Z_{\rm eff} = 2$ and 4.57. Letting only $Z_{\rm eff}$ vary, we predict $T_e({\rm warm})/T_e({\rm cryo}) = (4.57/2)^{2/7} = 1.27$. HYDRA simulation results in Fig. 3 roughly bear this out. T_e is higher in the warm simulation, especially in the LEH where all the beams overlap. Figure 3(b) shows the difference in T_e. This peaks at 600 eV in the LEH, where the cryo $T_e \approx 3$ keV, i.e., $T_e({\rm warm}) = 1.2T_e(\text{ cryo })$, is in line with our estimate.

III. BACKSCATTER AND THE CROSS BEAM ENERGY TRANSFER

In this section, we review the backscatter results from the warm and analogous cryo experiments. Results from warm shot N140313, when the outer beams were turned off before the inners, are used to develop a model for how the SRS reflectivity depends on the incident power. This SRS model is then applied to warm shot N140321, where the outers were kept on but the inner power was reduced, to develop a model for CBET. The SRS model is also applied to experiment N121226, which shows that $\Delta\lambda = 1.5$ Å gives CBET

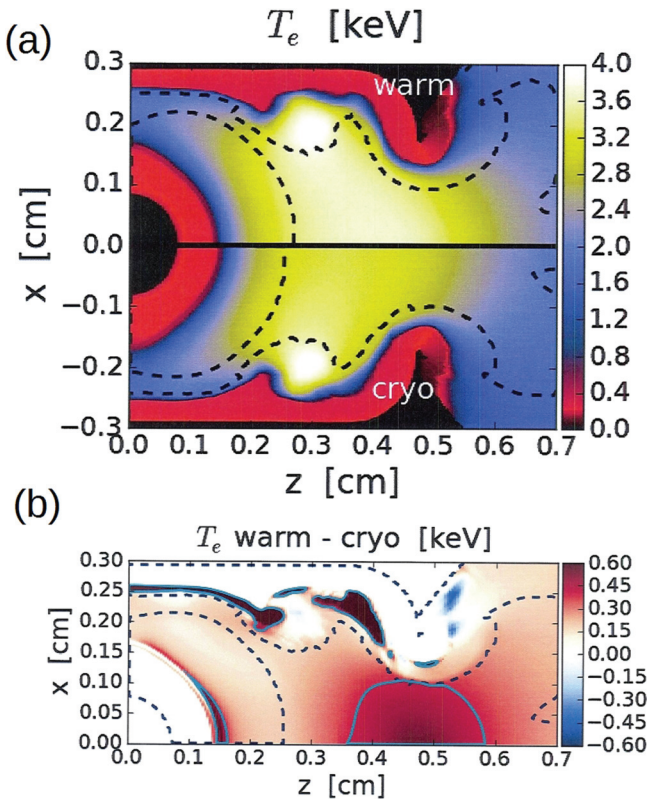

FIG. 3. Results of HYDRA simulations of NIF warm shot N130405, with no backscatter removed and no CBET (i.e., the nominal incident laser power). (a) Electron temperature at 19 ns (mid peak power) over one side ($z > 0$) of the hohlraum for warm (top) and cryo (bottom) gas fills. These are not proper simulations of the experiment, but are intended to illustrate the effect of gas composition. The dashed black contour is the boundary of the hohlraum fill gas. (b) Temperature difference $\Delta T_e = T_e(\text{warm}) - T_e(\text{cryo})$. Cyan contour is $\Delta T_e = 0.4$ keV.

close to zero for the warm platform. Finally, the post transfer intensity is used to determine the SBS threshold on the outers.

A. Backscatter diagnostics and energetics

Backscatter is measured on the NIF using the FABS and NBI diagnostics.[12] The SBS and SRS spectra and power histories are measured on the 30° and 50° cones using FABS, which measures the light reflected directly back into the beam lines. NBI scatter plates are on quads Q31B (30°), quads Q33B (23.5°), and Q36B (50°) inside the target chamber. These images are absolutely calibrated and provide a distribution of the scattered light outside the beam lines. The total energy is obtained through 2D fitting of the image. The absolute power measurements in FABS have an error of ±20% determined from the error in the energy measurement of the backscattered light on NBI used to constrain the power. This error shows up as an offset in the power time history of the backscattered signal with an additional error typically less than ±5% throughout the peak. In addition to FABS and NBI, the drive diagnostic sensors DrDs provide additional SBS backscatter results. This sensor is used to measure the laser energy and power on a shot to shot basis by sampling one beamline per quad except in 3 quads where all 4 beamlines are measured. These are the backscatter quads Q31B (30°) and Q36B (50°) as well as Q34T (50°). The SBS measurement results when the backscattered light partially (~2%) reflects off the frequency doubling crystal and is partially diverted by a transmission grating to the DrD sensor. This limits the SBS measurements to powers above roughly 50 TW per beamline because of the low level compared to the incident laser, but provides data on more beamlines.

Implosion symmetry was tuned in warm "symmetry capsule" (symcap) experiments using the wavelength shift $\Delta\lambda$ to control CBET. The inner cone fraction is $CF = P_{in}/(P_{out} + P_{in})$ where P_{in} and P_{out} are the average peak powers of the inner and outer beams respectively. $\Delta\lambda = 3.5$ Å was needed to minimize the P2 Legendre mode asymmetry in the hot spot in warm shots, compared to 5.5 Å in analogous cryo shots.

The measured backscatter energies are summarized in Table I. The overall coupling is defined as $C = 1 - E_{scat}/E_{LEH}$. The measured scattered energy on cone i is $E_{i,scat} = \int R_i(t)\sum_j P_j(t)dt$, summed over the quads on cone i, with reflectively $R_i(t) = P_{scat,i}(t)/P_{incident,i}(t)$ found on the quad with backscatter diagnostics on each cone (or estimated if none is measured, e.g., SRS on the 44.5° cone). The measured total scattered energy $E_{scat} = \sum_i E_{i,scat}$. E_{LEH} is the measured total laser energy at the LEHs. To provide context, the measured backscatter energy in Table I is given as a percent of the energy in the peak. The fraction of inner SRS increases from $(5\%, 12\%)$ for the $(23.5°, 30°)$ cones measured in experiment N121226, to 9% for the 23.5 s, and between 25% and 29% for the 30 s on the remaining experiments. The SRS increases due to the higher incident power, and increased the CBET since $\Delta\lambda$ was increased from 1.5 Å to 3.5 Å.

In the warm symcap experiments, the total coupling ranges from 90.8% to 92.9%. The warm shot N130405 produced a small Legendre-mode asymmetry P2 (defined below) in the hot spot with a total coupling of 91.7%. Similar P2 symmetry in cryogenic symcaps needed a higher $\Delta\lambda$ and resulted in reduced coupling between 85% and 89%. The vast majority of the backscatter from the cryo experiments was the inner cone SRS. Warm experiments have ~2.5× lower inner cone SRS reflectivity than cryo experiments with a similar capsule implosion symmetry. By contrast, the warm experiments had a significant 50° SBS. With frequencies close to the $3\omega_0$ laser frequency, SBS can damage optics. This risk limited the peak power in the warm experiments to full NIF powers <360 TW.

B. SRS and CBET measurement by pulse modification

In additional experiments designed to measure the CBET, the end of the laser pulse was modified and the resultant change in the inner cone SRS was measured. This technique has been used to measure CBET[13] at a specific time. Here we apply this method throughout the peak power. To motivate our empirical model, we start with the well-known Tang formula for the steady-state, plane-wave reflectivity in the strong damping limit[14]

TABLE I. Backscatter from the full-scale warm and cryo NIF experiments. Measurements taken from a combination of FABS, NBI, and DrDs. The highest error is in the 44.5° cone SRS since there is no measurement, the estimated value is equivalent to the 50° SRS with ±100% error. The 23.5° measurements use a limited cross shaped NBI scatter plate to determine the backscatter with an estimated error of ±40%. The 44.5° SBS measurements use a combination of 50° FABS and DrDs resulting in ±30% error. The remainder has ±20% error. Each measured energy value is represented as a percentage of the energy in the peak (above the half maximum power) of the laser pulse before transfer.

Shot number	N121226	N130125	N140207	N130217	N130405	N111109 (cryo)
$\Delta\lambda$ (Å)	1.5	3.5	3.5	3.5	3.5	5.5 (30°)/7.5 (23.5°)
Q33B SRS 23.5° (kJ)	0.72 (5%)	1.36 (9%)	1.27 (8%)	2.01 (9%)	2.07 (9%)	10.56 (50%)
Q33B SBS 23.5° (kJ)	0.13 (1%)	0.09 (1%)	0.15 (1%)	0.15 (1%)	0.24 (1%)	0.2 (1%)
Q31B SRS 30° (kJ)	1.6 (12%)	4.2 (29%)	4.33 (29%)	6.0 (29%)	5.5 (25%)	8.74 (41%)
Q31B SBS 30° (kJ)	0.04 (0%)	0.35 (2%)	0.47 (3%)	0.3 (1%)	0.3 (1%)	0.1 (0%)
Q36B SRS 50° (kJ)	0.01 (0%)	0.02 (0%)	0.03 (0%)	0.02 (0%)	0.01 (0%)	0.01 (0%)
Q36B SBS 50° (kJ)	2.0 (15%)	1.2 (8%)	1.17 (7%)	2.4 (11%)	2.05 (9%)	0.55 (3%)
44.5° SRS estimate (kJ)	0.01 (0%)	0.02 (0%)	0.034 (0%)	0.02 (0%)	0.01 (0%)	0.1 (0%)
44.5° SBS DrD (kJ)	0.4 (0%)	0.23 (2%)	0.23 (1%)	0.5 (2%)	0.41 (2%)	0.12 (1%)
Total backscatter (kJ)	58.4 ± 4.81	71.8 ± 8.3	70.4 ± 7.8	114.7 ± 12.3	104.6 ± 11.6	169.3
Laser energy (kJ)	821	946	957	1255	1266	1213
Peak power (TW)	291.5[a]	367.9	372.1	361.8	366.9	420.2
Coupling (%)	92.9 ± 1	92.4 ± 1	92.8 ± 1	90.8 ± 1	91.7 ± 1	86.0 ± 1

[a]Note that the peak power was 23.3% higher on Q23T (50°) and 45% higher on Q34T (50°) on N121226, this increase was offset by a dropped 23.5° quad (Q33T).

$$\tilde{R}(1-\tilde{R}+\tilde{s}) = \tilde{s}\exp[(1-\tilde{R})P_0 g]. \quad (8)$$

P_0 is the pump laser power, $\tilde{R} = (\omega_0/\omega_{SRS})R$, $R = P_{SRS}/P_0$, $\tilde{s} = (\omega_0/\omega_{SRS})P_{seed}/P_0$, g is the spatial gain rate per incident power, and P denotes power. In the large-gain limit $\tilde{s} \ll 1-\tilde{R} \ll 1$, this approximately gives

$$R_{SRS}(t) \approx R_{\max}\left[1 - \frac{P_{\rm thr}}{P_0(t)}\right]. \quad (9)$$

$R_{\max} \equiv \omega_{SRS}/\omega_0$ and $P_{\rm thr} \equiv \ln P_{seed}/g$. Eq. (9) was used in Ref. 13 with $R_{\max}$ and $P_{\rm thr}$ free parameters chosen to fit the experimental data. In our model, these depend on plasma conditions, but not on laser or SRS powers. We determine their values at one time on one experiment, and then apply them to other times and other experiments. The agreement with SRS data is decent, which validates our approach. The relatively small changes in SRS wavelength also gives some justification. $R_{\max} < \omega_{SRS}/\omega_0 \lesssim 0.65$ for the warm experiments, and can be even less due to the absorption of pump or scattered light, or nonlinear effects. $P_{\rm thr}$ plays the role of the threshold power for SRS. The SRS power is $P_{SRS} = R_{\max} \times (P_0 - P_{\rm thr})$. The temporal variation in P_0 and P_{SRS}, for instance due to amplitude modulations beam smoothing by spectral dispersion (SSD), is used to determine the coefficients after the outer beams are turned off.

We determine the parameters of the warm SRS model using the end of experiment N140313. The outer beams are turned off, so there is no CBET. This gives the black points in Fig. 4, which correspond to the best-fit values $P_{\rm thr} = 4.1$ TW and $R_{\max} = 0.33$. For comparison, the values published in Ref. 13 for similar cryo experiments were $P_{\rm thr} = 2.8$ TW and $R_{\max} = 0.29$. While this may indicate a lower gain due to plasma conditions in the warm experiments, the similarity in the spectra, shown in Fig. 5(c), signifies that the plasma conditions with the highest gain are similar.

We introduce a CBET model similar to Ref. 13. Assumptions similar to those made for SRS (plane-wave, steady-state, strong damping limit), and assuming small CBET, gives the approximate form

$$P_0 = P_{in}[1 + \gamma P_{out}], \quad (10)$$

where P_{in} and P_{out} are the incident inner and outer cone powers per quad. γ is the transfer rate from outers to the 30° inners, and depends on plasma conditions and $\Delta\lambda$. We determine γ using the end-of-pulse data for experiment N140321. We assume that CBET happens earlier along the laser path than SRS, so that the SRS power depends only on the post-transfer power P_0. In experiment N140321, the outers remain on, but the inner power is reduced. This results in a somewhat higher SRS power, which means that P_0 is slightly

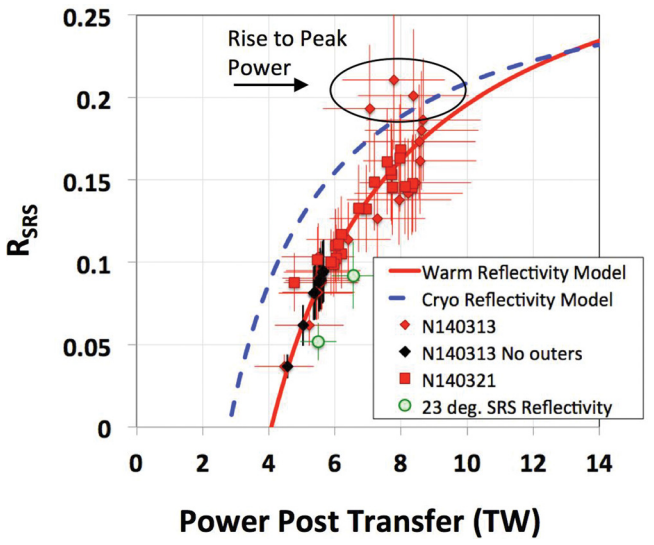

FIG. 4. The red and black points are the SRS reflectivity on 30° quad vs. calculated power post transfer. The solid red line is the SRS model determined from the warm experimental data shown in black with outer beams off. The red points indicate the SRS inner power taken with outer beams on. The dashed blue line was determined from cryo experiments and published in Ref. 13. The green circles are the average reflectivity of the 23.5° SRS vs. effective 30° quad power scaled the relative incident intensities.

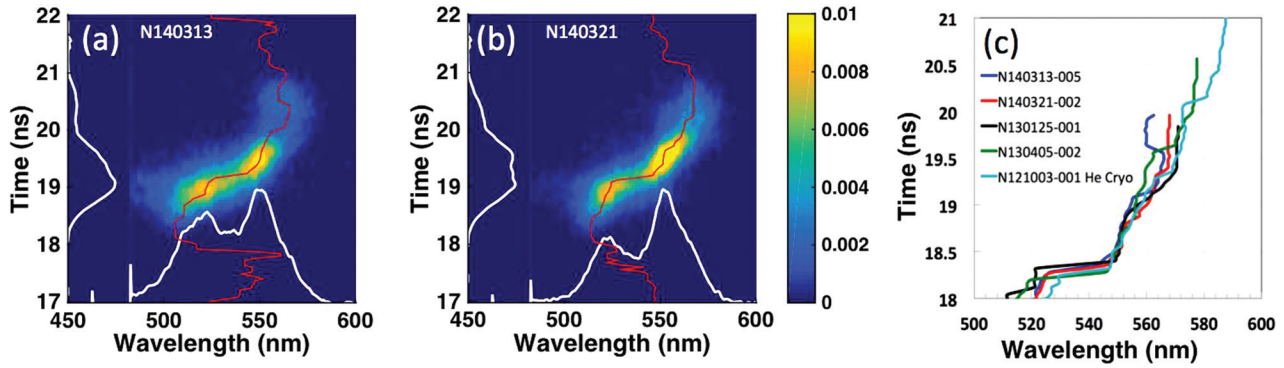

FIG. 5. (a) and (b) SRS streak spectrum from FABS measurements on 30° quad Q31B from two warm experiments shown in Fig. 4. White curves along side and bottom represent the corresponding normalized sum. The red line is the centroid wavelength (power weighted). (c) Centroid wavelength from several warm experiments, and cryo experiment N121003.

higher than at the end of experiment N140313. We thus find $\gamma = 0.095\ \mathrm{TW}^{-1}$ for this case of $\Delta\lambda = 3.5$ Å. This implies that, when all beams are at peak power, CBET increases the inner beam power by 51%. The cryo experiment considered in Ref. 13 used a larger $\Delta\lambda = 7.3$ Å and deduced a larger $\gamma = 0.135\ \mathrm{TW}^{-1}$. The SRS reflectivity data taken throughout the peak power is shown for the modified-pulse experiments in Fig. 4. The warm and cryo reflectivity models from Eq. (9) are plotted for comparison.

Additionally, while the signal levels were too low to make time resolved measurements for the 23.5° SRS, the average reflectivity in the peak is plotted for experiments N121226 and N130125. Here the average 23.5° quad power P_{ave23} has been scaled by the focal-spot areas of the beams to get an effective power that would give the same intensity on a 30° quad: $P_{23effective} = A_{30s}/A_{23.5s} \times P_{ave23}$ with $A_{30s}/A_{23.5s} = 1.14$. The 23.5° SRS data are close to the reflectivity model for 30° SRS, assuming no net CBET to the 23.5° cone. The resulting cone fraction, *CF*, in the peak of the pulse after CBET and backscatter are accounted for that was 41 ± 1.5% in the warm experiments with $\Delta\lambda$ 3.5 Å (N130125) and remained at 33 ± 1% for $\Delta\lambda$ 1.5 Å (N121226).

Experimental results and comparison with our model are shown in Fig. 6. The blue [dashed, solid] curve is the [Q31B (30°), Q36B (50°)] incident quad power. The red filled curve is the measured Q31B SRS power. Figure 6(a) shows the effect of turning off the outer cones on the inner 30° SRS. The SRS power is 65% the value when the outer beams are on. The SRS power from the warm SRS model (Eq. (9)) is shown in Figs. 6(a) and 6(b) in solid black. One of the sources of error associated with this model is the ±100 ps temporal jitter of the laser powers. This jitter could explain the divergence of the SRS model in (a) if the inner and outer pulse shapes were slightly mistimed. The warm SRS model is applied to another warm experiment in Fig. 6(b) in which the inner-beam power was reduced by 20% at the end. Agreement between the measured SRS power and the simple model indicates a good understanding of CBET for these experiments.

Finally, we use this model to confirm that CBET was minimized in the warm shot N121226, with lower $\Delta\lambda = 1.5$ Å. This was chosen to minimize CBET by compensating for the flow-induced Doppler shift between the inner and outer beams. The measured SRS power is shown in Fig. 6(c), along with the results of our SRS model with no CBET ($\gamma = 0$). The measured SRS wavelength in this shot (not shown) was similar to N140313, which supports using the same model values. Over the peak of the pulse, the average SRS power from the model of 0.78 ± 0.08 TW was very close to the measured value 0.76 ± 0.08 TW. The model over predicted SRS by 3.0%, well within the experimental error bars. We conclude that the measured SRS is consistent with little to no CBET

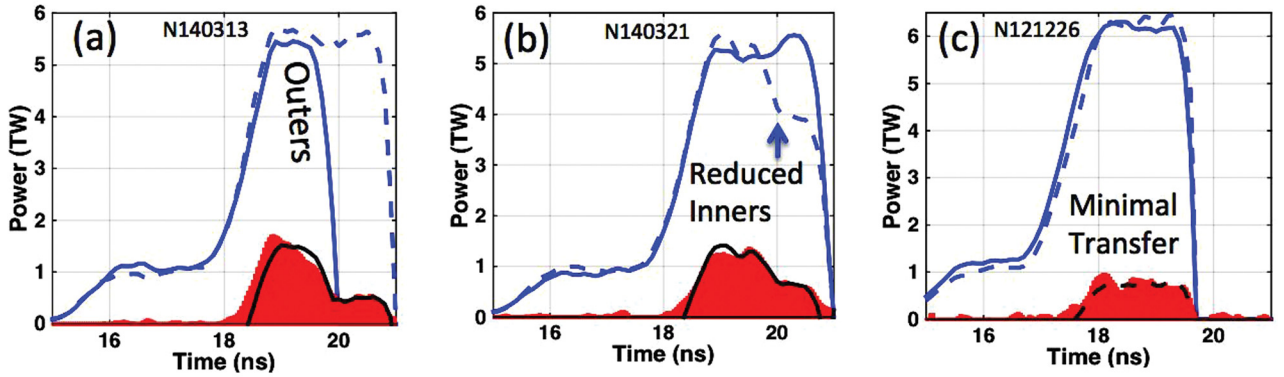

FIG. 6. Data from end-of-pulse experiments used to determine the inner SRS and CBET models. (a) Results of N140313 where the outer pulse was truncated in time compared to the inner pulse. The (dashed, solid) blue curves are the incident powers of the (30°, 50°) quads. Red filled is the measured SRS on 30° quad Q31B. Solid black line is the estimate for SRS based on Eqs. (9) and (10). (b) Results for N140321 where inner beams are reduced at the end of the pulse. (c) Results for experiment N121226 with SRS calculated assuming no CBET ($\gamma = 0$).

during the peak power in this experiment, and that flow-induced CBET can be compensated by $\Delta\lambda$.

C. SRS spectra

The SRS scattered wavelength is a function of the electron density and temperature at the resonance location, where the thermal noise is amplified to a finite level. There can still be significant off-resonant growth as the SRS light continues to propagate, as indicated by reduced modeling of SRS in rad-hydro simulations.[15] SRS occurs through scattering from the electron plasma wave, with a linear dispersion relation $\omega_p^2 \approx \omega_{pe}^2 + 3v_e^2 k_p^2$ where k_p is the wave number and $\omega_{pe} \equiv [n_e e^2/\epsilon_0 m_e]^{1/2}$ is the electron plasma frequency. The electron thermal velocity $v_e \equiv [T_e/m_e]^{1/2}$ establishes the temperature dependence. The incident and scattered light are related by energy and momentum conservation: $\omega_0 = \omega_s + \omega_p$, $\vec{k}_0 = \vec{k}_s + \vec{k}_p$.

Comparing the SRS spectra can establish if SRS develops from similar plasma conditions. Figs. 5(a) and 5(b) show the spectra at the end of pulse experiments, N140313 and N140321, respectively, and correspond to Figs. 6(a) and 6(b). The spectral centroids from several warm shots are plotted vs. time in Fig. 5(c). The peak of the laser pulse was delayed by roughly 800 ps in N140313 and N140321 compared to the symcap experiments to delay the shocks, so these spectra have been shifted to align the start of the rise to peak power. The cryo symcap, N121003, is shown for comparison. Note the similarity of the warm and cryo spectra. The variation in SRS wavelengths occurring before the steep shift at rise to peak power ~18.3 ns may indicate that the variation in plasma conditions before the peak was larger than during the peak. After the jump to approximately 548 nm, the variation in the spectra is within 2 nm and begins to widen slightly with time. In the warm shot N140313, there is a noted increase in wavelength of 6 nm at 19.1 ns when the outers are truncated. The shift is in the same direction but less than the observed shift in cryo experiments of 9 nm and is followed by a decrease at 19.6 ns. This could indicate plasma cooling without the additional heating from outer beams.

The centroid of the SRS spectrum from the cryo shot N121003 is shown for comparison in cyan in Fig. 5(c). This shot used a longer peak pulse with a peak power of 390 TW, and a 3-color scheme $(\lambda_{23.5}, \lambda_{30}) - \lambda_{\text{out}} = (9.7, 6.5)$ Å. Despite the differences in the laser pulse, the gas fill and the CBET, the SRS spectra of the cryo falls within the variation in the measurements from the warm experiments, suggesting that the SRS may develop from similar plasma conditions. The initial jump from 520 nm to 550 nm to an additional ~20 nm also occurs in both the warm and cryo experiments with similar movement in spectra in time after the jump.

D. Outer-beam SBS data

The SBS power history measured in several warm symcap experiments is plotted in Fig. 7(a). These experiments ramped up to a peak energy of 1.27 MJ by first increasing the power in the peak and then by extending the peak power in time. The difference in SBS power between the first two experiments is small, even though the incident power increased. This is because the 2nd shot used a higher $\Delta\lambda$ and had more CBET from outer to inner beams.

The outer-beam SBS spectra from a typical warm and cryo shot are shown in Figs. 7(b) and 7(d). The outer cone SBS in such cryo experiments typically rises only near the end of the laser pulse. We do not measure where in space the SBS light develops, so we cannot say, on a strictly experimental basis where the SBS occurs. We discuss this issue by considering SBS from a resonant ion acoustic wave in a single ion species plasma. The SBS wavelength is approximately

$$\lambda_{SBS} - \lambda_0 \approx 7.3\text{Å}\,\tilde{c}_a(1+M) \qquad M \equiv \frac{\vec{u}\cdot\hat{k}_0}{c_a}, \tag{11}$$

where we assume 351 nm laser light, $\tilde{c}_a^2 = (ZT_e + 3T_i)/A$, temperatures are in keV, $c_a = \tilde{c}_a m_u^{1/2}$ is the acoustic speed, and $\vec{u}$ is the plasma flow velocity. Using gold wall blowoff parameters consistent with simulations of $Z = 50$, $T_e = 3$ keV, $ZT_e \gg 3T_i$, and $M = -0.6$, we find $\lambda_{SBS} - \lambda_0 =$ 2.2 Å. The shift is higher in lower Z regions with higher acoustic speeds, like the hohlraum fill gas. One conclusion is that the measured SBS wavelengths seem to require significant flow opposite the laser $\vec{k}_0$. Others have attributed (short, long) wavelength SBS to (high, low) Z plasma, e.g., Ref. 16, which reports previous neopentane-filled hohlraum experiments on the OMEGA laser. The spatial origin of outer-beam SBS is not clear, and is the subject of ongoing work. We note the possibility that a finite "seed" from the gold wall can be further amplified in the fill gas.

To determine the scaling of outer SBS reflectivity with intensity, three different 50° pulse shapes were used in N121226 with differing peak intensities. In addition, the 50° and 44.5° cones use Continuous Phase Plates (CPPs) with different focal spot sizes. The resulting focal intensity of the 50° quads is roughly 14% higher than the 44.5° quads with the same power, providing an additional scaling data. This is plotted in Fig. 7(c), along with another warm shot with higher peak power and larger $\Delta\lambda$ (N130125). We assume the plasma conditions for the 44.5 s and 50 s are the same because they point at the same z position along the wall. The SRS CBET model described above was used to determine the post transfer intensity for the outers. From the data, the SBS appears to increase dramatically for intensity $\gtrsim 9 \times 10^{14}$ W/cm^2.

Lastly, we compare the SBS reflectivity between warm and cryo experiments. Here we compare our SBS measurements from FABS from the warm experiment with low CBET (N121226), with a cryo experiment with large CBET and in which the inners were truncated in time (N120622). The last 400 ps of the outer pulse in this cryo experiment has no CBET since the inners are off, allowing an outer SBS reflectivity measurement at that time. Since the pulse lengths are different, we compare the SBS 1.5 ns after the start of the peak power as shown in Fig. 8. The 50° quad Q36B in the cryo experiment at 20.9 ns had an incident power of 5.65 TW and a SBS power of 0.92 ± 0.18 TW, giving a SBS reflectivity of $16.2 \pm 3.2\%$. The warm experiment at time 19.4 ns had an incident power of 5.9 TW and a SBS power of 0.83 ± 0.17 TW, giving a reflectivity of $14.0 \pm 3\%$. These reflectivities are similar within the errors.

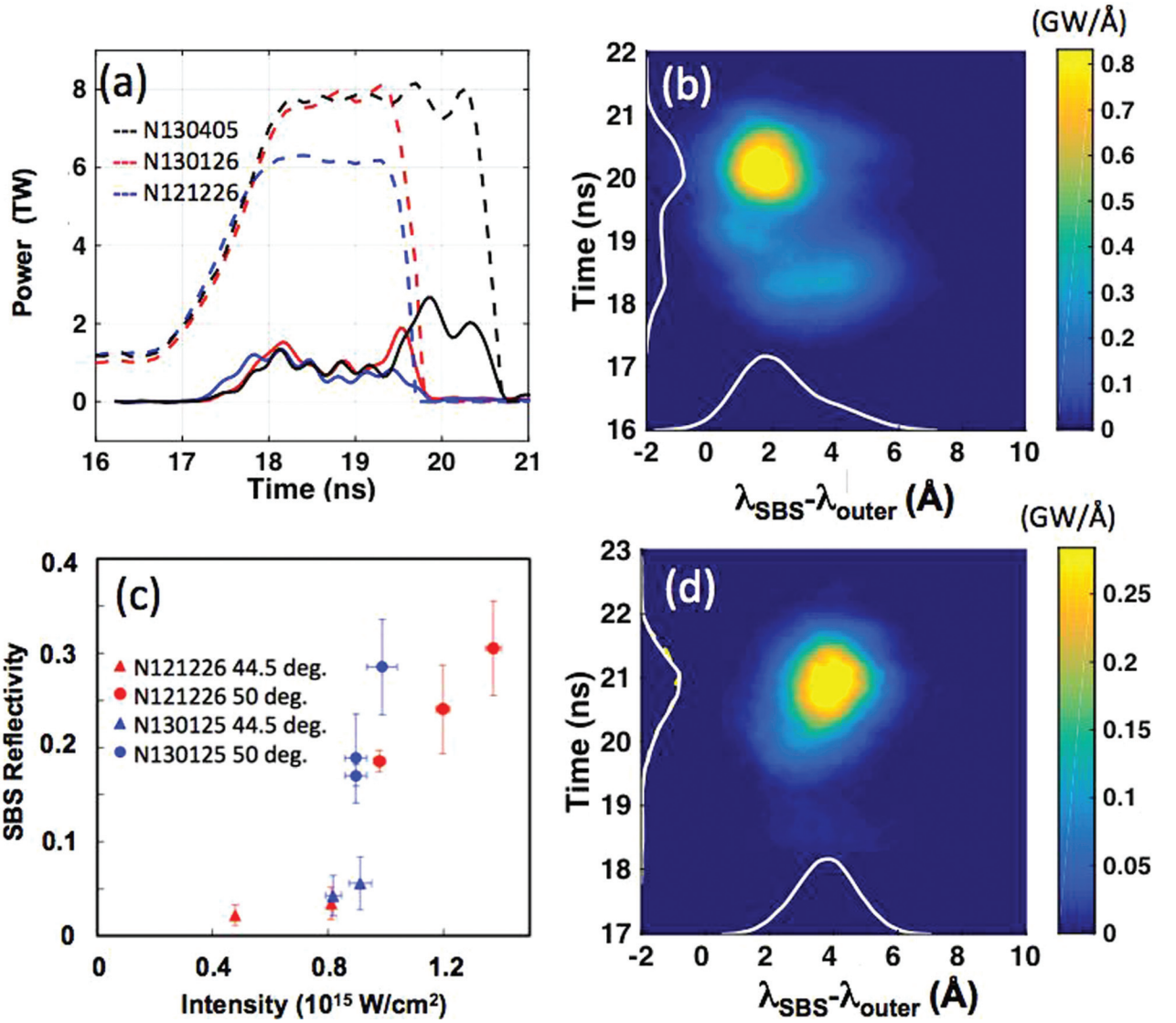

FIG. 7. (a) Q36B (50°) FABS quad laser power during peak power (dashed), and measured SBS power (solid), in 3 warm symcap experiments. The (blue, red, black) curves are from (N121226, N130125, and N130405). (b) and (d) are streaked SBS spectra from (b) N130405 and a similar cryo shot (d) N130424. (c) SBS reflectivity from N121226 (blue) and N130125 (red) from outer cone DrDs. Triangles are from 44.5° beams, and circles are from 50° beams.

IV. SYMMETRY EXPERIMENTS

In this section, the results of the warm symmetry experiments are reviewed. They primarily show that in warm hohlraums, a lower $\Delta\lambda$ is required to minimize the oblateness of the x-ray self emission from the capsule hot spot. However, the implosion shape is shown to scale with $\Delta\lambda$ with roughly the same slope as in the cryo experiments. Measurements using the static x-ray camera are shown to scale consistently with the CBET model found from the backscatter data allowing for a calibration of the hard x-ray flux with laser intensity. These experiments also show that the radiation temperature T_{rad} is higher in the warm experiments by 5 to 7 eV when compared to cryo experiments with similar absorbed laser energy, or roughly an additional 1 TW/sr of total x-ray flux.

A. Implosion self-emission shape

The symmetry capsule ("symcap") experiments are designed to produce implosions with symmetry equivalent to DT implosions.[17] The CH capsules were all nominally 208 μm thick with a layer of 1% Si dopant and a radius of 0.9 mm. These capsules are thicker than the DT layered capsules to emulate the effect of the DT layer.[5] In these experiments, the shape of the self emission from the hot compressed gas in the capsule is measured using the x-ray framing cameras.[18] Two cameras are fielded on symcap experiments, one located at the equator and one at the pole. The equatorial camera measures the shape of the hot spot through a high density carbon window on the side of the hohlraum, which allows x-rays with energies <20 keV to pass unimpeded by the 30 μm Au hohlraum wall. The 10× pinhole imaging provides a spatial resolution of 10 μm and a temporal resolution of roughly 75 ps. The camera filtering and timing are set up to measure the bright 6 to 12 keV x-ray emission near the peak compression.

The implosion shape is typically characterized using the Legendre mode decomposition of the 17% brightness contour. From the equator, this contour radius is

TABLE II. Summary of the shape data for full-scale warm and cryo experiments.

Shot number	N121226	N130125	N130217	N130405	N111109 (cryo)
$\Delta\lambda$ (Å)	1.5	3.5	3.5	3.5	7.5 (23.5 s)/6.0 (30 s)[a]
Hot spot P0 (μm)	41.4 ± 4.1	60.5 ± 1.6	52.7 ± 1.46	65.0 ± 1.8	50.6 ± 2.8
Hot spot P2/P0 (%)	−60.8 ± 5.4	−4 ± 3.2	−22.6 ± 1.4	−3.3 ± 2.7	1.6 ± 0.4
Hot spot P4/P0 (%)	NA	−7.8 ± 6.5	−6.0 ± 3.7	21 ± 3.7	−4.7 ± 1.4
Hot spot M0 (μm)	No data	No data	71.5 ± 1.4	83.0 ± 0.7	58.5 ± 3.4
Hot spot M4/M0 (%)	No data	No data	1.7 ± 1.1	2.1 ± 0.1	3.2 ± 0.8
Peak T_{RAD} (eV)	275.4 ± 6.9	283.0 ± 7.1	304.3 ± 7.6	301.4 ± 7.5	NA
Peak x-ray flux (TW/sr)	10.8	11.9	15.9	15.3	NA

[a]Cryo shot used a 3-color $\Delta\lambda$ to transfer more power to the 23.5° beams.

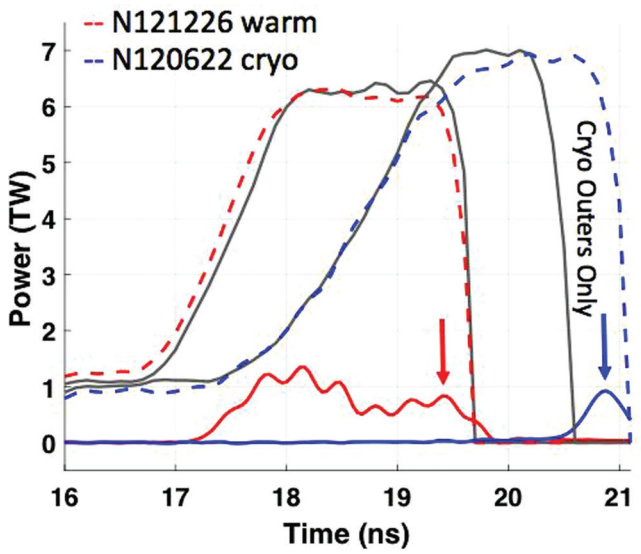

FIG. 8. Comparison of outer SBS in warm and cryo experiments. The dashed curves are the power history of Q36B. The gray curves are the corresponding 30° power. The (red, blue) curves are from (warm experiment N121226, cryo experiment N120622). The solid curves are the Q36B FABS SBS power measurements. Arrows mark times of the reflectivities, are compared in the text.

$S(\theta) = \Sigma_n A_n P_n(\cos\theta)$ with $A_n = \int P_n S d\theta$ and P_n the order n Legendre polynomial. Similarly the polar GXD images are decomposed into Fourier m-modes $S(\phi) = \Sigma_n M_n \exp(in\phi)$. X-ray drive near the equator is determined by the incident power of the inner beams, laser plasma interactions, and absorption along the path. In gas filled hohlraums, CBET is used to move power between cones to tune the equatorial P modes and azimuthal m-modes. The P2 mode defines whether the implosion is prolate (P2 > 0) or oblate (P2 < 0).[18] No attempt was made to correct the polar shape in these experiments, so we do not report m-modes here.

Table II presents the implosion shape data for four warm symcap shots, all in hohlraums with a nominal length of 9.43 mm, LEH diameter of 3.373 mm, and an identical beam pointing. Cryo symcap shot N111109 is included for comparison, which used a 3-color scheme: $(\lambda_{23.5}, \lambda_{30}) - \lambda_{out} = (7.5, 6.0)$ Å. Images of the hot spot self-emission at peak x-ray emission are shown in Fig. 9. The white line is the 17% contour used to determine the Legendre modes. Only the first, low-energy warm shot N121226 used $\Delta\lambda = 1.5$ Å. This was designed to minimize the CBET, and resulted in P2/P0 = −60.8%. The next warm shot N130125 increased $\Delta\lambda$ to 3.5 Å, increased peak power, and resulted in a nearly round implosion with P2/P0 = −4%. We extended the peak power on N130405, and also obtained a nearly round implosion with P2/P0 = 3.3%.

Figure 10 compares the variation of P2 with $\Delta\lambda$ for warm and cryo shots. The cryo shots used hohlraums with lengths from 9.325 mm to 9.425 mm, total laser energies from 1.24 MJ to 1.5 MJ, total peak power from 391 TW to 446 TW, and a 3-color scheme with $\lambda_{23.5} - \lambda_{30}$, between 1 and 1.5 Å. In the 3 color scheme, energy is transferred between the inner ones from the 30° to the 23.5° beams for additional symmetry control. Simulations adjusted to match the P2 data are plotted in black, and guided P2 tuning via $\Delta\lambda$ in the warm shots. The P2 data for warm shots are offset from the cryo shots: less $\Delta\lambda$ is needed to produce the same P2. But the slopes are similar. The minimum hot spot P2 for the warm platform occurs at $\Delta\lambda \gtrsim 3.5$ Å, compared to ≈6 Å needed for the cryo platform.

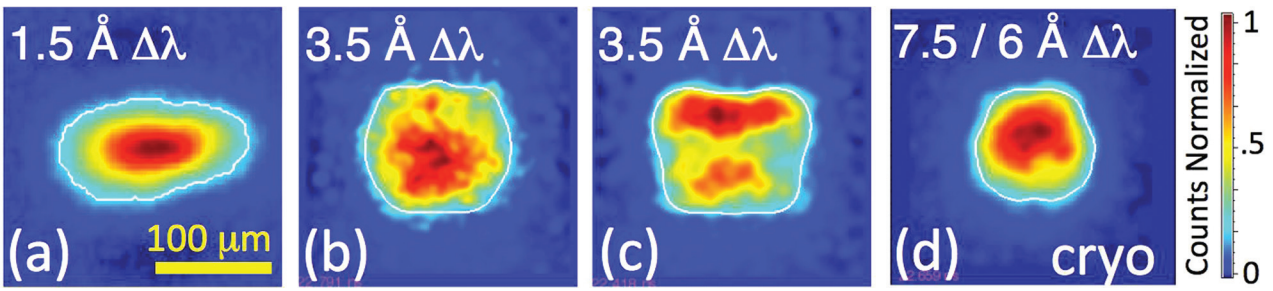

FIG. 9. Equatorial GXD images of the hot spot self-emission at time of peak x-ray emission from warm symcap shots (a) N121226, (b) N130125, (c) N130405, and (d) similar cryo shot N111109. Each shot's $\Delta\lambda$ is at the top of each image. Experiment details are in Table II.

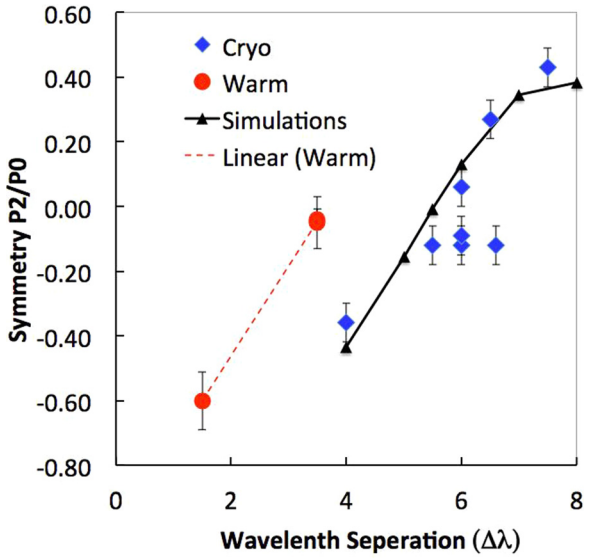

FIG. 10. P2/P0 vs. $\Delta\lambda = \lambda_{30s} - \lambda_{outers}$ for warm (red) and cryo (blue) symcap shots. Black curve shows the results of cryo simulations including CBET. λ_{30s} and λ_{outers} are the wavelengths corresponding to the fundamental 1ω 30° cone and outers (44.5° and 50°).

B. Hard x-ray images of the inner surface of the hohlraum

Images from the static x-ray imager (SXI) can indicate the relative intensity and location of the beams on the hohlraum wall. In Fig. 11, a 3D depiction using the commercial software VISRAD shows the laser power deposited from the viewpoint of lower SXI. The hohlraum wall is shown as a grid from the outside, allowing us to see through it and view the power deposited by the beams inside. The SXI view is limited to what can be seen through the LEH (highlighted in dashed red). Below, the SXI images are compared side-by-side. They show the interior wall of the hohlraum looking through the LEH at 19° off the z axis[19] providing a spatial image of the 3 to 5 keV x-rays with a spatial resolution of ~60 μm. The soft x-ray channel, with a center energy of 870 eV (not shown) near the peak of the Planckian of a 300 eV blackbody is used to determine the clear aperture for the DANTE analysis presented in this paper.

Fig. 11 shows the relative brightness of x-rays emitted where the beams strike the wall. The warm shot N130405 has a thicker outer beam ring and a smaller dark region between the far outer Q23T and the far inner (23.5°) Q26T. In the 3 keV channel of the SXI, to first order, the brightness $B \propto \int I_{wall}(t)dt$ resulting in a fluence, where $I_{wall} = I_0 \cos(\theta)$ is the intensity on the wall. θ is incidence angle on the wall estimated in this case by the initial incidence angle before wall motion. Fig. 11 shows the average inferred fluence on the wall as a function of SXI average counts (brightness) at 3 keV for several warm symcap shots. The inferred fluence is found using the CBET model described in Sec. III B. The nearly linear relation between the x-ray counts for the inner and outer beams in SXI and the inferred fluence on the wall further supports the SRS CBET model. Fig. 12 shows that

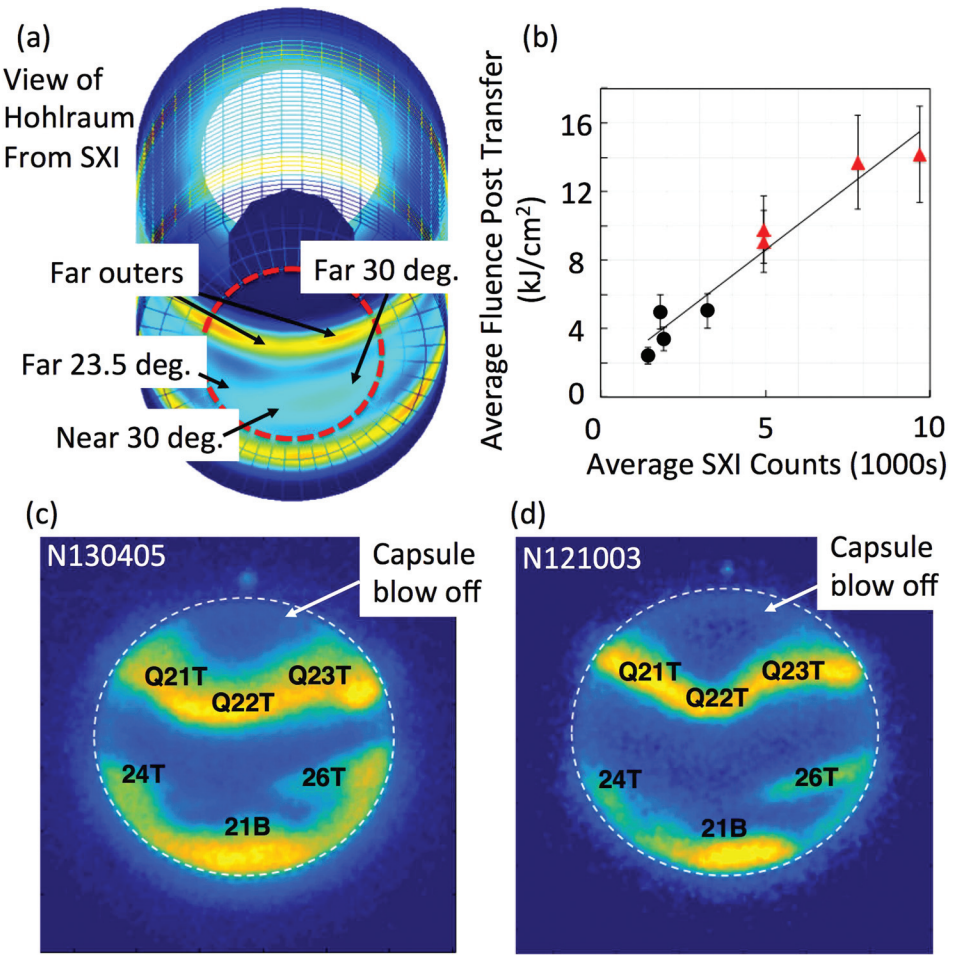

FIG. 11. (a) VISRAD image showing the view of the hohlraum and beam spots relative to the LEH. (b) Inferred laser fluence on the hohlraum wall vs. the SXI counts for inner (black circles) and outer (red triangles) beam spots. Solid line is best fit to the data. (c) SXI image for the 3 keV channel for warm shot N130405, and (d) similar cryo shot N121003. The labeled visible quads and their cone angle are: Q21T and Q23T (upper 50°), Q22T (upper 44.5°), Q24T (upper 23.5°), Q26T (upper 30°), Q21B (lower 30°). Dashed curves are elliptic fits to the outer LEH edge.

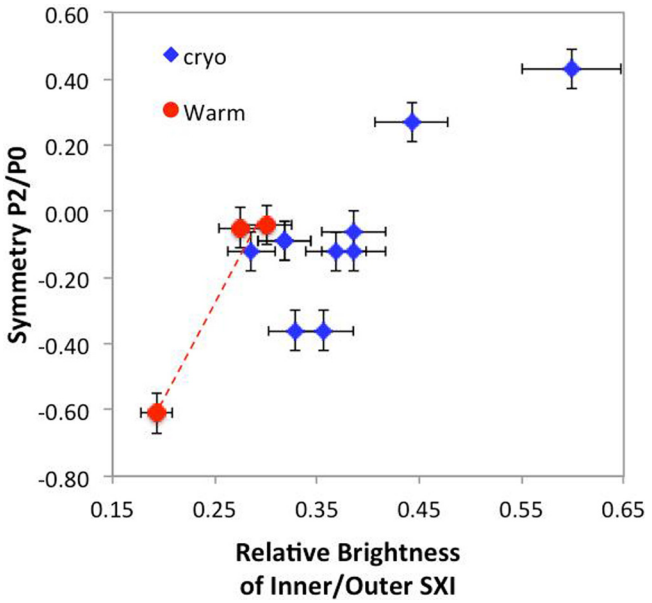

FIG. 12. P2/P0 from hot-spot self-emission vs. the relative x-ray brightness between the inners and outers as measured by SXI.

the warm and cryo shots have a similar correlation between P2 and inner vs. the outer SXI brightness. This indicates that the same laser illumination pattern on the wall produces the same P2 shape in both platforms.

C. Time history of hot spot shape near the peak compression

The time history of the hot spot shape for warm shot N130405 is shown in Fig. 13. While the absolute measure of P2/P0 at peak x-ray emission was small (−3.3%), there is a rapid time-dependent "swing" through peak emission: $\Delta P2/\Delta T = 38.5 \pm 3.7\,\mu$m/ns. Ideally, the swing would be negligible. The P4 swing is also considerable, starting negative and continuing to get more negative: $\Delta P4/\Delta T = -35.2 \pm 1.1\,\mu$m/ns. Compensating for P4 usually entails repointing the beams within the hohlraum or changing the hohlraum length.

D. Radiation drive

Fig. 14 compares the absolute x-ray drive of the hohlraum as measured by the DANTE diagnostic.[20–22] DANTE measured the time history and spectra of the x-ray emission through the LEH. Here the inferred $T_{\rm rad}$ satisfies $\sigma T_{\rm rad}^4 = \pi f_{clear} \Phi / A_{clear} \cos\theta$, where Φ is the x-ray flux from the LEH, f_{clear} is the fraction of flux coming from inside the LEH, and σ is the Stefan-Boltzmann constant. The error in (Φ, $T_{\rm rad}$) is ($\pm 5\%$, $\pm 1.5\%$) during the peak. A_{clear} is the area based on the hard aperture measured with the SXI.

Figure 14 shows a comparison of the warm experiments with the entire set of cryo hohlraum experiments with the same hohlraum and 4 shock pulse shapes. The data indicates that warm hohlraum reaches slightly higher temperatures than comparable cryo hohlraums. The highest $T_{\rm rad}$ of 304.3 ± 7.5 eV was reached with an incident laser energy 1.14 MJ after subtracting the backscatter and used a nominally 360 TW peak power laser pulse. The warm drive is on average 3–7 eV higher than the cryo experiments plotted. Including the error in the measurement, this puts the warm hohlraums just inside the error bars of the highest performing cryo experiments.

Another measure of the x-ray drive produced in the hohlraum is the implosion "coast time" $T_c \equiv T_{bt} - T_{off}$ where T_{bt} is time of peak x-ray brightness, and T_{off} is the end of the laser pulse (which typically is the time of peak $T_{\rm rad}$). The variation in the cryo data results because the time of peak capsule x-ray emission and the velocity of the capsule are a function of the experimental parameters as well as the hohlraum drive. Nevertheless, T_c is similar for similar peak $T_{\rm rad}$ in the warm and cryo platforms.

V. SUBSCALE 2D CONVERGENT ABLATOR COMPARISON EXPERIMENTS

In a pair of experiments we directly compare the warm and cryo hohlraum implosions using the same laser pulse and $\Delta\lambda$. The laser pulse and hohlraum were reduced-scale versions of the experiments described in all preceding sections. The approach is to design a hydrodynamically equivalent capsule implosion. This entails scaling physical lengths

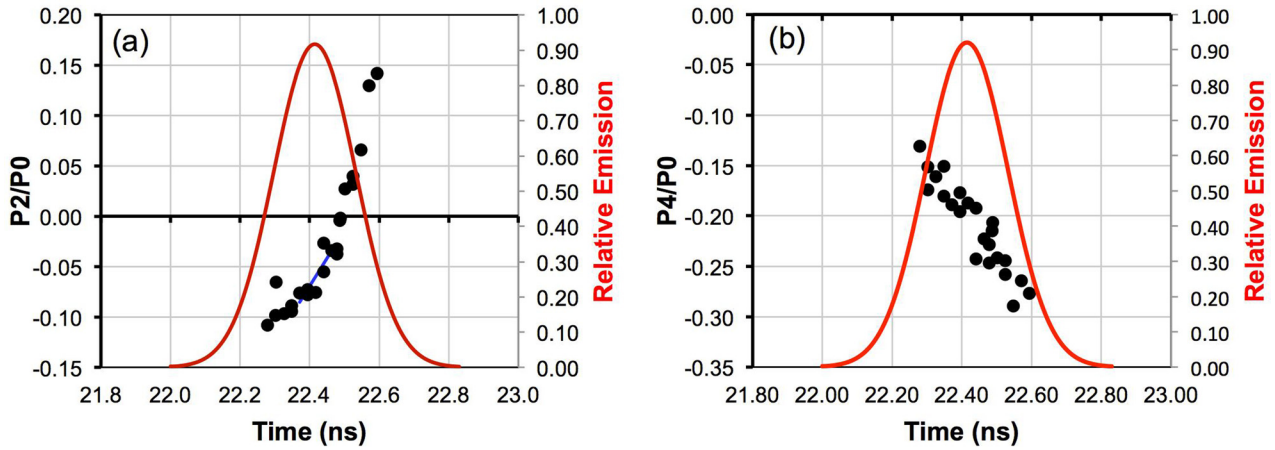

FIG. 13. Time resolved hot spot shape from warm shot N130405. (a) P2/P0 is plotted in black. (b) P4/P0 plotted in black. Red solid curves are normalized total emission. The P2/P0 data in Table II corresponds to the P2 at peak x-ray emission, and images in Fig. 9 are at times nearest to peak x-ray emission.

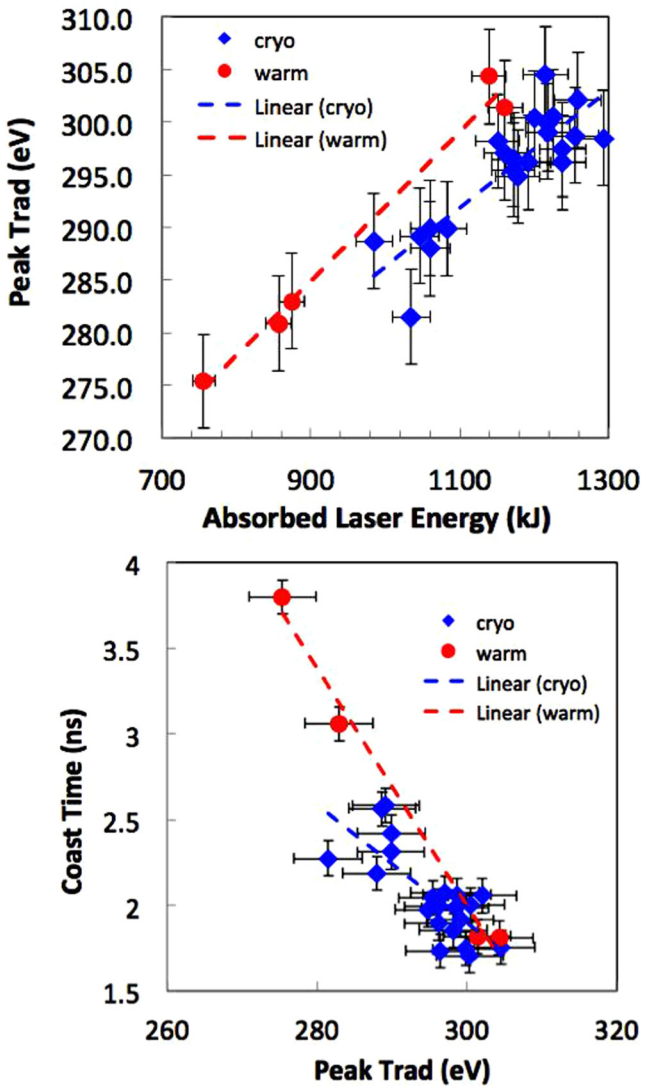

FIG. 14. (a) Peak T_{rad} for warm and cryo NIF shots with similar size hohlraums. The x-axis is the coupled laser energy = incident minus escaping backscatter. The (red circles, blue diamonds) represent (warm, cryo) shots. The blue and red dashed lines are linear fits to the data.

(hohlraum and capsule sizes) by a scale factor s, laser pulse time by s, and laser power by s^2. This preserves the energy density in the hohlraum. On NIF, we typically do not scale the LEH size strictly with s, or the laser spot sizes (determined by the phase plates) at all. The subscale shots used $s = 0.81$, resulting in a reduced hohlraum diameter of 4.67 mm (compared to the full-scale 5.75 mm). The LEH diameter was 3.1 mm, as shown in Fig. 15. The hohlraums were heated using a 17.25 ns, 4-shock pulse (shown in the inset in Fig. 15) with a total energy summing over all 184 target beams at the LEH of 868 kJ. In the 2D convergent ablator (2D ConA) experiments such as these, two quads are diverted to a germanium plate to produce x-rays used for backlighting the implosion. The backlighter pulse is timed to match the peak velocity of the imploding capsule, and is shown in the laser pulse inset red dashed in Fig. 15. The hohlraum and capsule gas fills were identical to the full scale experiments. The subscale experiments used a 3-color scheme to balance the drive between the 23.5° and 30° beams: $(\lambda_{23.5}, \lambda_{30}) - \lambda_{out} = (4.7, 3.5)$ Å.

The results of the subscale experiments support the findings of previous sections. Table III shows the measured backscatter of the subscale experiments. The total inner beam backscatter on the two shots agree to within the experimental error, but differ slightly in the distribution among the inner beams. The cryo experiment had evenly distributed the SRS among the inner cones, while the 23.5° cone had 1.82× the SRS of the 30° cone in the warm experiment. This indicates that CBET between cones might be different between the warm and cryo experiments. Note that the accuracy of the 23.5° SRS measurements are significantly improved in these subscale experiments after a diagnostic upgrade compared to the full scale experiments described earlier.

The primary measurements of these experiments were radiographs of the in-flight shell shape and are shown in Fig. 16 when the capsule radius P0 = 200 μm, around the peak velocity. The 2D ConA experiments use the equatorial framing camera along with a backlighter to radiograph the shape and velocity of the imploding shell.[23] In these experiments, the shell trajectory of 295 km/s was similar between the two experiments, and consistent with the same laser coupling measured. However, the warm shot showed a larger positive P2 = 16.9±2 μ m compared to the cryo shot with P2 = 10.7±2μ m. This difference could indicate a combination of either improved inner beam propagation or more transfer in the warm experiment as compared with the cryo experiment. Higher modes were negligible in both cases.

At peak compression, the hot spot shape from x-ray self-emission was comparable: P0 = (37, 39) μm and P2 = (2,4) μm for (warm, cryo). There was a larger P2 shape swing in the warm shot (from +17 μm at P0 = 200 μm to 2 μm at peak compression) than the cryo (+11 μm at P0 = 200 μm to 4 μm at peak compression). This swing in shape is again attributable to the differences in the temporal hohlraum flux due to the improved inner beam propagation or more transfer. The small P2 swing measured during the backlit radiographs was well within the analysis variation.

The subscale shape results are consistent with the full scale experiments, where P2 was minimized at a lower $\Delta\lambda$ than for similar cryo experiments. At the same $\Delta\lambda$, we would expect and indeed measured a higher P2 in the warm shot. Likewise, the SRS difference between the inner cones in the warm experiment could indicate that more transfer occurs between the inner cones at the same inner $\Delta\lambda = \lambda_{23.5s} - \lambda_{30s} = 1.2$ Å. Reducing the CBET through a reduction in both the inner to outer and 3-color $\Delta\lambda$ may lead to a decrease in the total inner SRS and help to improve the overall coupling in the warm hohlraum while improving the P2. Finally, the measured peak radiation temperature of 295.8 eV in the warm subscale experiment was higher than the cryo value of 290.0 eV by ~6 eV, for almost the same coupled laser energy. This is again consistent with the full-scale results.

VI. SUMMARY

The room-temperature or warm hohlraum platform has been successfully commissioned on NIF, and is in use. Results of a series of full-scale warm experiments have been

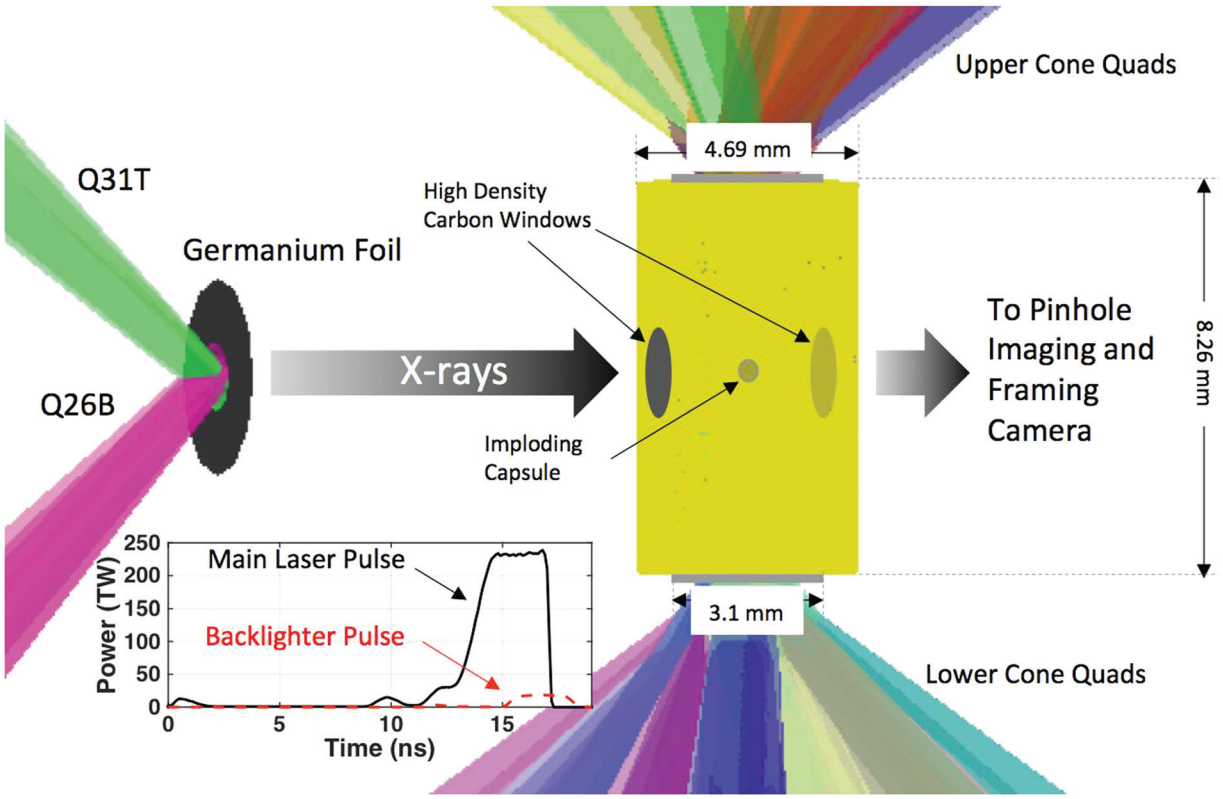

FIG. 15. Setup for subscale 2D ConA experiments. 50° quads Q31T and Q26B are used to excite germanium K_α emission. The x-rays pass through the HDC windows in the hohlraum providing a time-resolved radiograph of the imploding shell near peak velocity.

TABLE III. Backscatter for NIF subscale experiments.

Shot number	N140712 warm	N140913 cryo
Q33B SRS (23.5°) (kJ)	2.64 ± 0.5	2.06 ± 0.4
Q33B SBS (23.5°) (kJ)	0.29 ± 0.06	0.18 ± 0.04
Q31B SRS (30°) (kJ)	1.45 ± 0.3	1.97 ± 0.4
Q31B SBS (30°) (kJ)	0.07 ± 0.01	0.23 ± 0.04
Inner SRS (kJ/quad)	2.05 ± 0.3	2.02 ± 0.3
Q36B SRS (50°) (kJ)	0.01 ± 0.00	0.02 ± 0.00
Q36B SBS (50°) (kJ)	1.19 ± 0.4	1.2 ± 0.24
44.5° SRS estimate (kJ/quad)	0.01 ± 0.01	0.02 ± 0.02
44.5° SBS (DrD) (kJ/quad)	0.26 ± 0.07	0.29 ± 0.07
Total backscatter (kJ)	89.6 ± 4.8	93.8 ± 8.3
Laser energy (kJ)	866.9	881.5
Coupling (%)	89.7 ± 1	89.4 ± 1

presented, along with a subscale warm-cryo direct comparison. The experimental evidence suggests that the warm platform has some performance improvements compared to cryo hohlraums. Hydrodynamic simulations indicate that the higher Z hohlraum gas fill (neopentane) in the warm platform results in up to 20% higher electron temperature in the LEH, due to the increased IB absorption and reduced electron thermal conductivity. The different plasma conditions lead to measured differences in backscatter and implosion shape, and inferred differences in the CBET for a given wavelength shift $\Delta\lambda$.

Measurements of the backscatter from the end of pulse experiments indicate that the intensity threshold for significant inner SRS is higher in the warm experiments compared to cryo. Using an SRS model allowing for pump depletion,

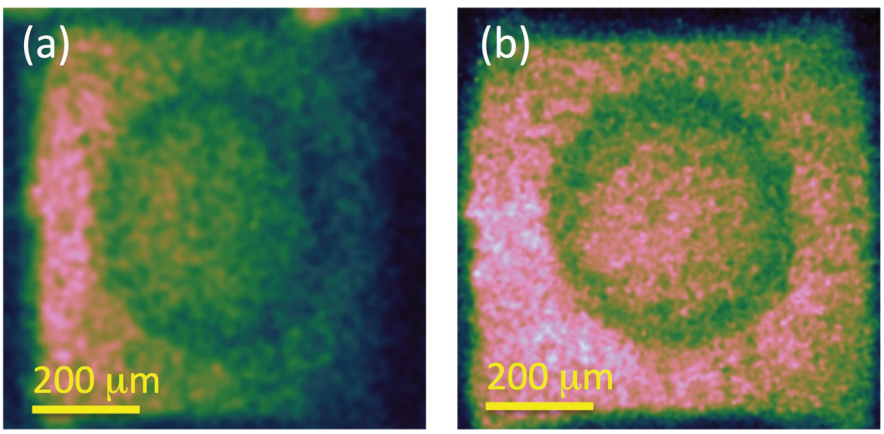

FIG. 16. Radiographs of the imploding capsules from warm and cryo subscale 2D ConA experiments when P0 = 200 μm. >(a) Warm experiment N140712 with measured P2 = 16.9 ± 2 μm. (b) Cryo experiment N140913 with P2 = 10.7 ± 2 μm.

12±2% of the power in the outers was diverted to the inners through CBET in the warm experiments with $\Delta\lambda$ 3.5 Å corresponding to a peak inner cone fraction post transfer and after subtracting backscatter of 41 ± 1.5%. A detailed analysis of the SXI data indicates an intensity trend with a brightness between the inner and outer spots on the interior wall of the hohlraum consistent with the CBET inferred using the SRS method. Additionally, $\Delta\lambda = 3.5$ Å was needed to minimize the P2 shape of the hot spot self emission at peak x-ray brightness in the warm shape experiments, which is less than the 6 Å needed in similar cryo experiments. This suggests an improvement in the inner beam propagation and/or more CBET at lower $\Delta\lambda$.

A pair of subscale warm and cryo direct comparison experiments was conducted with the same 3-color scheme. These 2D ConA experiments produced a more prolate implosion in the warm hohlraum at a capsule radius of 200 μm. The warm and cryo shots gave the same total inner cone SRS. This result is consistent with an improved inner beam propagation in the warm platform. The data suggests that shape tuning can be accomplished with a lower inner cone fraction when using a hohlraum with a higher $\langle Z \rangle$ fill. Finally, the x-ray flux produced by warm hohlraums is 5 to 7 eV higher than the typical cryogenic hohlraums after accounting for backscatter (i.e., for the same coupled laser energy).

ACKNOWLEDGMENTS

This work provides the physics basis for new uses of the warm gas filled hohlraum platform on the NIF with a laser energy exceeding 1 MJ. The results indicate that the warm platform could be used for surrogate implosion experiments on new designs with a high x-ray drive. Additionally, the relative simplicity of fielding of this platform will allow for more complicated experiments such as the planned magnetized hohlraum experiments and others. This work was performed under the auspices of the U.S. Department of Energy by Lawrence Livermore National Laboratory under Contract No. DE-AC52-07NA27344.

[1]A. J. Mackinnon, J. L. Kline, S. N. Dixit, S. H. Glenzer, M. J. Edwards, D. A. Callahan, N. B. Meezan, S. W. Haan, J. D. Kilkenny, T. Döppner, D. R. Farley, J. D. Moody, J. E. Ralph, B. J. MacGowan, O. L. Landen, H. F. Robey, T. R. Boehly, P. M. Celliers, J. H. Eggert, K. Krauter, G. Frieders, G. F. Ross, D. G. Hicks, R. E. Olson, S. V. Weber, B. K. Spears, J. D. Salmonsen, P. Michel, L. Divol, B. Hammel, C. A. Thomas, D. S. Clark, O. S. Jones, P. T. Springer, C. J. Cerjan, G. W. Collins, V. Y. Glebov, J. P. Knauer, C. Sangster, C. Stoeckl, P. McKenty, J. M. McNaney, R. J. Leeper, C. L. Ruiz, G. W. Cooper, A. G. Nelson, G. G. A. Chandler, K. D. Hahn, M. J. Moran, M. B. Schneider, N. E. Palmer, R. M. Bionta, E. P. Hartouni, S. LePape, P. K. Patel, N. Izumi, R. Tommasini, E. J. Bond, J. A. Caggiano, R. Hatarik, G. P. Grim, F. E. Merrill, D. N. Fittinghoff, N. Guler, O. Drury, D. C. Wilson, H. W. Herrmann, W. Stoeffl, D. T. Casey, M. G. Johnson, J. A. Frenje, R. D. Petrasso, A. Zylestra, H. Rinderknecht, D. H. Kalantar, J. M. Dzenitis, P. Di Nicola, D. C. Eder, W. H. Courdin, G. Gururangan, S. C. Burkhart, S. Friedrich, D. L. Blueuel, L. A. Bernstein, M. J. Eckart, D. H. Munro, S. P. Hatchett, A. G. Macphee, D. H. Edgell, D. K. Bradley, P. M. Bell, S. M. Glenn, N. Simanovskaia, M. A. Barrios, R. Benedetti, G. A. Kyrala, R. P. J. Town, E. L. Dewald, J. L. Milovich, K. Widmann, A. S. Moore, G. LaCaille, S. P. Regan, L. J. Suter, B. Felker, R. C. Ashabranner, M. C. Jackson, R. Prasad, M. J. Richardson, T. R. Kohut, P. S. Datte, G. W. Krauter, J. J. Klingman, R. F. Burr, T. A. Land, M. R. Hermann, D. A. Latray, R. L. Saunders, S. Weaver, S. J. Cohen, L. Berzins, S. G. Brass, E. S. Palma, R. R. Lowe-Webb, G. N. McHalle, P. A. Arnold, L. J. Lagin, C. D. Marshall, G. K. Brunton, D. G. Mathisen, R. D. Wood, J. R. Cox, R. B. Ehrlich, K. M. Knittel, M. W. Bowers, R. A. Zacharias, B. K. Young, J. P. Holder, J. R. Kimbrough, T. Ma, K. N. La Fortune, C. C. Widmayer, M. J. Shaw, G. V. Erbert, K. S. Jancaitis, J. M. DiNicola, C. Orth, G. Heestand, R. Kirkwood, C. Haynam, P. J. Wegner, P. K. Whitman, A. Hamza, E. G. Dzenitis, R. J. Wallace, S. D. Bhandarkar, T. G. Parham, R. Dylla-Spears, E. R. Mapoles, B. J. Kozioziemski, J. D. Sater, C. F. Walters, B. J. Haid, J. Fair, A. Nikroo, E. Giraldez, K. Moreno, B. Vanwonterghem, R. L. Kauffman, S. Batha, D. W. Larson, R. J. Fortner, D. H. Schneider, J. D. Lindl, R. W. Patterson, L. J. Atherton, and E. I. Moses, "Assembly of high-areal-density deuterium-tritium fuel from indirectly driven cryogenic implosions," Phys. Rev. Lett. **108**, 215005 (2012).

[2]R. L. Kauffman, L. J. Suter, C. B. Darrow, J. D. Kilkenny, H. N. Kornblum, D. S. Montgomery, D. W. Phillion, M. D. Rosen, A. R. Theissen, R. J. Wallace, and F. Ze, "High temperatures in inertial confinement fusion radiation cavities heated with 0.35μm light," Phys. Rev. Lett. **73**, 2320–2323 (1994).

[3]R. Sigel, R. Pakula, S. Sakabe, and G. D. Tsakiris, "X-ray generation in a cavity heated by 1.3- or 0.44-μm laser light. iii. comparison of the experimental results with theoretical predictions for x-ray confinement," Phys. Rev. A **38**, 5779–5785 (1988).

[4]E. Moses, J. Lindl, M. Spaeth, R. Patterson, R. Sawicki, L. Atherton, P. Baisden, L. Lagin, D. Larson, B. MacGowan *et al.*, "Overview: Development of the national ignition facility and the transition to a user facility for the ignition campaign and high energy density scientific research," Fusion Sci. Technol. **69**, 1–24 (2016).

[5]S. W. Haan, J. D. Lindl, D. A. Callahan, D. S. Clark, J. D. Salmonson, B. A. Hammel, L. J. Atherton, R. C. Cook, M. J. Edwards, S. Glenzer, A. V. Hamza, S. P. Hatchett, M. C. Herrmann, D. E. Hinkel, D. D. Ho, H. Huang, O. S. Jones, J. Kline, G. Kyrala, O. L. Landen, B. J. MacGowan, M. M. Marinak, D. D. Meyerhofer, J. L. Milovich, K. A. Moreno, E. I. Moses, D. H. Munro, A. Nikroo, R. E. Olson, K. Peterson, S. M. Pollaine, J. E. Ralph, H. F. Robey, B. K. Spears, P. T. Springer, L. J. Suter, C. A. Thomas, R. P. Town, R. Vesey, S. V. Weber, H. L. Wilkens, and D. C. Wilson, "Point design targets, specifications, and requirements for the 2010 ignition campaign on the national ignition facility," Phys. Plasmas **18**, 051001 (2011).

[6]A. Pak, E. L. Dewald, O. L. Landen, J. Milovich, D. J. Strozzi, L. F. Berzak Hopkins, D. K. Bradley, L. Divol, D. D. Ho, A. J. MacKinnon, N. B. Meezan, P. Michel, J. D. Moody, A. S. Moore, M. B. Schneider, R. P. J. Town, W. W. Hsing, and M. J. Edwards, "Laser absorption, power transfer, and radiation symmetry during the first shock of inertial confinement fusion gas-filled hohlraum experiments," Phys. Plasmas **22**, 122701 (2015).

[7]M. M. Marinak, G. D. Kerbel, N. A. Gentile, O. Jones, D. Munro, S. Pollaine, T. R. Dittrich, and S. W. Haan, "Three-dimensional HYDRA simulations of National Ignition Facility targets," Phys. Plasmas **8**, 2257–2280 (2001).

[8]M. Rosen, H. Scott, D. Hinkel, E. Williams, D. Callahan, R. Town, L. Divol, P. Michel, W. Kruer, L. Suter, R. London, J. Harte, and G. Zimmerman, "The role of a detailed configuration accounting (DCA) atomic physics package in explaining the energy balance in ignition-scale hohlraums," High Energy Density Phys. **7**, 180–190 (2011).

[9]N. B. Meezan, L. J. Atherton, D. A. Callahan, E. L. Dewald, S. Dixit, E. G. Dzenitis, M. J. Edwards, C. A. Haynam, D. E. Hinkel, O. S. Jones, O. Landen, R. A. London, P. A. Michel, J. D. Moody, J. L. Milovich, M. B. Schneider, C. A. Thomas, R. P. J. Town, A. L. Warrick, S. V. Weber, K. Widmann, S. H. Glenzer, L. J. Suter, B. J. MacGowan, J. L. Kline, G. A. Kyrala, and A. Nikroo, "National ignition campaign hohlraum energetics," Phys. Plasmas **17**, 056304 (2010).

[10]D. E. Hinkel, D. A. Callahan, N. B. Meezan, L. J. Suter, C. H. Still, D. J. Strozzi, E. A. Williams, and A. B. Langdon, "Analyses of laser-plasma interactions in NIF ignition emulator designs," J. Phys.: Conf. Ser. **244**, 022019 (2010).

[11]NIF shots are labeled in the format YYMMDD for the shot date.

[12]J. D. Moody, P. Datte, K. Krauter, E. Bond, P. A. Michel, S. H. Glenzer, L. Divol, C. Niemann, L. Suter, N. Meezan, B. J. MacGowan, R. Hibbard, R. London, J. Kilkenny, R. Wallace, J. L. Kline, K. Knittel, G. Frieders, B. Golick, G. Ross, K. Widmann, J. Jackson, S. Vernon, and T. Clancy, in *18th Topical Conference on High-Temperature Plasma Diagnostics, Wildwood, NJ, 16–20 May 2010* ["Backscatter measurements for NIF ignition targets (invited)," Rev. Sci. Instrum. **81**, 10D921 (2010)].

[13]J. D. Moody, D. J. Strozzi, L. Divol, P. Michel, S. LePape, J. Ralph, J. S. Ross, S. H. Glenzer, R. K. Kirkwood, O. L. Landen, B. J. MacGowan, A. Nikroo, and E. A. Williams, "Raman backscatter as a remote laser power sensor in high-energy-density plasmas," Phys. Rev. Lett. **111**, 025001 (2013).
[14]C. L. Tang, "Saturation and spectral characteristics of the stokes emission in the stimulated Brillouin process," J. Appl. Phys. **37**, 2945–2955 (1966).
[15]D. J. Strozzi, D. S. Bailey, P. Michel, L. Divol, S. M. Sepke, G. D. Kerbel, C. A. Thomas, J. E. Ralph, J. D. Moody, and M. B. Schneider, "Interplay of laser-plasma interactions and inertial fusion hydrodynamics," Phys. Rev. Lett. (to be published).
[16]P. Neumayer, R. L. Berger, D. Callahan, L. Divol, D. H. Froula, R. A. London, B. J. MacGowan, N. B. Meezan, P. A. Michel, J. S. Ross, C. Sorce, K. Widmann, L. J. Suter, and S. H. Glenzer, in *49th Annual Meeting of the Division of Plasma Physics of the American-Physical-Society, Orlando, FL, 12–16 November 2007* ["Energetics of multiple-ion species hohlraum plasmas," Phys. Plasmas **15**(5), 056307 (2008)].
[17]G. A. Kyrala, J. L. Kline, S. Dixit, S. Glenzer, D. Kalantar, D. Bradley, N. Izumi, N. Meezan, O. Landen, D. Callahan, S. V. Weber, J. P. Holder, S. Glenn, M. J. Edwards, J. Koch, L. J. Suter, S. W. Haan, R. P. J. Town, P. Michel, O. Jones, S. Langer, J. D. Moody, E. L. Dewald, T. Ma, J. Ralph, A. Hamza, E. Dzenitis, and J. Kilkenny, "Symmetry tuning for ignition capsules via the symcap technique," Phys. Plasmas **18**, 056307 (2011).
[18]G. A. Kyrala, S. Dixit, S. Glenzer, D. Kalantar, D. Bradley, N. Izumi, N. Meezan, O. L. Landen, D. Callahan, S. V. Weber, J. P. Holder, S. Glenn, M. J. Edwards, P. Bell, J. Kimbrough, J. Koch, R. Prasad, L. Suter, J. L. Kline, and J. Kilkenny, in *18th Topical Conference on High-Temperature Plasma Diagnostics, Wildwood, NJ, 16–20 May 2010* ["Measuring symmetry of implosions in cryogenic Hohlraums at the NIF using gated x-ray detectors (invited)," Rev. Sci. Instrum. **81**, 10E316 (2010)].
[19]M. B. Schneider, O. S. Jones, N. B. Meezan, J. L. Milovich, R. P. Town, S. S. Alvarez, R. G. Beeler, D. K. Bradley, J. R. Celeste, S. N. Dixit, M. J. Edwards, M. J. Haugh, D. H. Kalantar, J. L. Kline, G. A. Kyrala, O. L. Landen, B. J. MacGowan, P. Michel, J. D. Moody, S. K. Oberhelman, K. W. Piston, M. J. Pivovaroff, L. J. Suter, A. T. Teruya, C. A. Thomas, S. P. Vernon, A. L. Warrick, K. Widmann, R. D. Wood, and B. K. Young, "Images of the laser entrance hole from the static x-ray imager at NIF," Rev. Sci. Instrum. **81**(10), 10E538 (2010).
[20]R. L. Kauffman, H. N. Kornblum, D. W. Phillion, C. B. Darrow, B. F. Lasinski, L. J. Suter, A. R. Theissen, R. J. Wallace, and F. Ze, "Drive characterization of indirect drive targets on the nova laser (invited)," Rev. Sci. Instrum. **66**, 678–682 (1995).
[21]E. L. Dewald, K. M. Campbell, R. E. Turner, J. P. Holder, O. L. Landen, S. H. Glenzer, R. L. Kauffman, L. J. Suter, M. Landon, M. Rhodes, and D. Lee, "Dante soft x-ray power diagnostic for national ignition facility," Rev. Sci. Instrum. **75**, 3759–3761 (2004).
[22]J. L. Kline, K. Widmann, A. Warrick, R. E. Olson, C. A. Thomas, A. S. Moore, L. J. Suter, O. Landen, D. Callahan, S. Azevedo, J. Liebman, S. H. Glenzer, A. Conder, S. N. Dixit, P. Torres, V. Tran, E. L. Dewald, J. Kamperschroer, L. J. Atherton, R. Beeler, L. Berzins, J. Celeste, C. Haynam, W. Hsing, D. Larson, B. J. MacGowan, D. Hinkel, D. Kalantar, R. Kauffman, J. Kilkenny, N. Meezan, M. D. Rosen, M. Schneider, E. A. Williams, S. Vernon, R. J. Wallace, B. Van Wonterghem, and B. K. Young, "The first measurements of soft x-ray flux from ignition scale hohlraums at the national ignition facility using dante (invited)," Rev. Sci. Instrum. **81**, 10E321 (2010).
[23]J. R. Rygg, O. S. Jones, J. E. Field, M. A. Barrios, L. R. Benedetti, G. W. Collins, D. C. Eder, M. J. Edwards, J. L. Kline, J. J. Kroll, O. L. Landen, T. Ma, A. Pak, J. L. Peterson, K. Raman, R. P. J. Town, and D. K. Bradley, "2d x-ray radiography of imploding capsules at the national ignition facility," Phys. Rev. Lett. **112**, 195001 (2014).